WILEY-VCH

DOI: 10.1002/ ((please add manuscript number))
Article type: Full Paper

Superior Mechanical and Magnetic Performance of Highly Anisotropic Sendust Flake Composites Freeze Cast in a Uniform Magnetic Field

*Kaiyang Yin, Bradley A. Reese, Charles R. Sullivan, and Ulrike G.K. Wegst**

((Optional Dedication))

Dr. Kaiyang Yin, Prof. Ulrike G.K. Wegst
Department of Physics, Northeastern University, Boston, Massachusetts 02115, USA
E-mail: u.wegst@northeastern.edu

Dr. Kaiyang Yin, Dr. Bradley A. Reese, Prof. Charles R. Sullivan, Prof. Ulrike G.K. Wegst
Thayer School of Engineering, Dartmouth College, Hanover, NH, 03755, United States

Keywords: flake alignment, monodomain structure, permeability, quality factor

Despite extensive research, the manufacture in bulk of high-performance flake-based magnetic composites with a highly aligned, nacre-like structure remains challenging. Many challenges can be overcome by freeze casting in an externally applied, uniform magnetic field, which causes both the flakes and the composite walls of the cellular solid to align parallel to the B-field lines. When appropriately sized, the flakes experience a second alignment parallel to the freezing direction because of a shear flow that occurs due to both the volumetric expansion of the ice phase and mold contraction during the directional solidification. The resulting orthotropic structure of the freeze-cast magnetic composite is reflected in orthotropic mechanical and magnetic properties of the material. The magnetic composites manufactured by magnetic-field assisted freeze casting outperform by a factor of 2-4 in terms of stiffness, strength, and toughness materials that were processed in the absence of a magnetic field and do not exhibit a monodomain architecture. Because of the highly aligned microstructure, it is possible to compact the initially lamellar composite with 90% porosity to at least 80% strain. The results presented in this study illustrate the tremendous potential for magnetic freeze casting of magnetic composites for use in power conversion.

1. Introduction

Traditionally, power losses in magnetic core materials are reduced by interleaving thin layers of a magnetic material with thin layers of an electrical insulator. When a time varying magnetic flux passes through a conductor (including many magnetic materials), eddy currents are generated, which lead to power loss. Thin laminations of magnetic material decrease the amount of flux passing through a conductive region, thus reducing the magnitude of induced eddy currents. While emerging thin-film magnetic materials offer significantly lower power losses than ferrites in the 1-100 MHz range, they are very expensive to manufacture and difficult to scale up to higher power levels [1].

Instead of continuous laminations, some cores are composed of small magnetic particles embedded in an insulating binder. Commercially available powder cores are composed of individually insulated magnetic particles that are approximately 100 μm in size and offer lower losses than laminated tape wound cores, but higher losses than ferrites [2]. An alternative approach to achieve low power loss at high frequency, while maintaining lower cost and better scalability than thin films, are composite materials composed of magnetic flakes, such as those composed of Sendust (**Figure 1**A) embedded in an insulating binder [3–8].

Advantages of magnetic flakes are that they not only have a low eddy current loss due to their small cross-sectional area but that their performance can further be improved by precise alignment [8]. Several studies focused on composite cores manufactured with magnetic flakes of thicknesses in the 100-500 nm range. Since the cross-sectional area of these flakes is so small, they allow for a significant reduction of eddy current loss. However, for best performance, the flakes must be precisely aligned with the magnetic field. In fact, misalignment not only increases power loss, but could additionally result in localized heating and thermal stresses on the component.

To date, flake-based composites have been formed around a winding, as shown in Figure 1B with flakes aligned (a) with a magnetic field generated from the winding and (b) by

applying pressure to the assembly [9]. With pressure, a better alignment of the flakes could be achieved than with the magnetic field alignment, however, there were still large regions which were not aligned correctly, and the performance peaked at 4 MHz. In an alternative approach, bare cores (i.e., without an embedded winding) were hot pressed resulting in a better flake alignment [3].

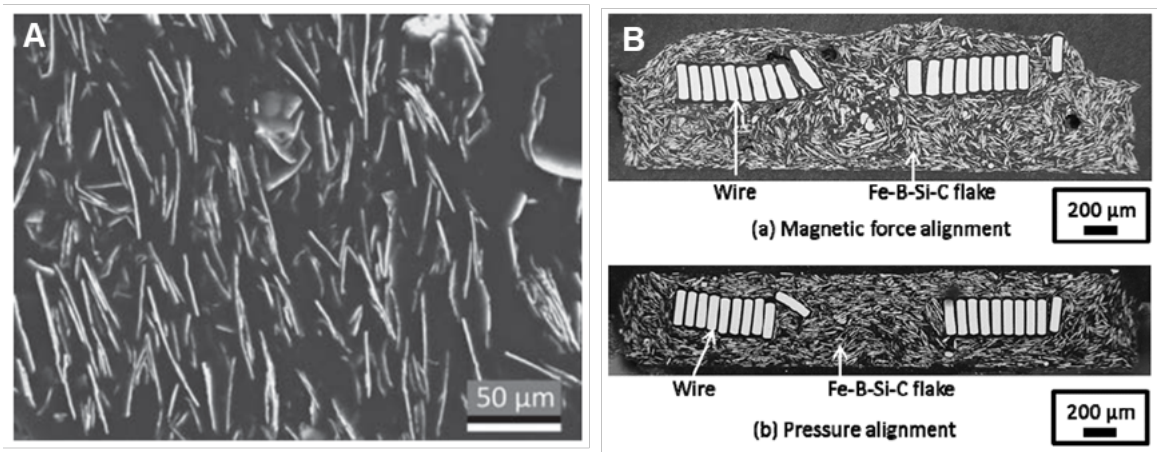

Figure 1. (A) SEM micrograph of Sendust flakes (50 µm diameter, 2 µm thickness). Reproduced with permission. [10] 2018, IEEE. (B) SEM micrograph of the magnetic flake composite of Endo et al. (2015). Reproduced with permission. [9] 2015, IEEE.

Permeabilities achieved with these flake-based materials started to roll off at approximately 10 MHz. The materials of Shirakate et al. (2008) [5] and Suetsuna et al. (2016) [4] had very good, yet still imperfect particle alignment after hot pressing, which led to permeability rolloff at 100 MHz and 1 GHz, respectively. Combined, these results highlight that the performance of flake-based magnetic composites is highly dependent on the quality of flake alignment, and that there is still room for improvement. Thus, processes, with which a better control of flake alignment can be achieved, could greatly extend the capability of magnetic components.

A novel and highly promising approach for the manufacture of low loss magnetic composites with highly aligned flakes is freeze-casting [11–19]. Freeze casting, also termed ice-

templating, is based on the directional solidification of water-based particle slurries [20–24]. Initially, the process was shown to produce highly aligned, nacre-like microstructures with alumina platelets in a polymer binder[23]. The platelet–polymer composite forms, when the water-based slurry solidifies directionally and dendrites of pure ice grow in the direction of the temperature gradient. Nacre-like lamellae self-assemble in the interdendritic spaces because of an interdendritic shear flow, which is caused by the volumetric expansion of the ice phase. The shear flow forces the flakes to align with their long dimension parallel to the freezing direction to then be 'glued' by the polymer phase [23]. Additionally, multiple studies have been performed to investigate alignment effects of an externally applied magnetic field on paramagnetic spheres, rods, and flakes of different shapes, including magnetic nanoparticle-decorated alumina platelets.[25–39]

Combining the process of ice templating with the application of an externally applied magnetic field, it could be shown that the structural alignment of particles surface magnetized with magnetic nanoparticles (MNP) could, indeed, be further modified, and that their properties could be custom-designed. [11,18,19]. Applying, for example, a static external magnetic field during the solidification of MNP-decorated alumina particles and platelets resulted in 60% of the cell walls aligning with the field [19]; freeze casting titania in a rotating magnetic field resulted in a helical sample architecture [16]. However, investigating the magnetic freeze casting system used in these studies further, it became apparent that the magnetic flux in the round mold was not uniform. As a result, the surface-magnetized particles were not only rotated but also translated and thus concentrated toward the magnetic fixture, which is an undesirable effect for our application and therefore needed to be eliminated.

Inspired by these earlier results, we chose as our approach to the manufacture of magnetic composites to freeze cast low loss magnetic flakes, suspended in an electrically insulating and, optimally, also thermally conducting binder to alter thermal performance, in an externally applied uniform magnetic field. The goal was to achieve a monodomain material

architecture, in which nacre-like lamellae composed of highly aligned magnetic flakes are aligned both parallel to the freezing direction and, perpendicular to it, parallel to the applied magnetic field. The objective was to explore the promise of magnetic freeze casting as a route for the manufacture of flake-based magnetic composites with reduced eddy current losses, for which currently no suitable, cost-effective manufacturing process exists.

2. Results

2.1. Structural Characterization

2.1.1 Density and Volume Fractions

In the frozen state, the dimensions of the freeze-cast magnetic composite are 15.6 mm × 15.6 mm, both when manufactured in the presence or the absence of a magnetic field. Lyophilizing the samples results in dimensional shrinkage (**Table 1**). In the case of the composite freeze-cast without a B-field, the two cross-sectional dimensions shrink by 5.3% to 14.77 ± 0.06 mm and by 7.1% to 14.49 ± 0.23 mm, respectively. When freeze-cast in the presence of a B-field the shrinkage is larger perpendicular to the B field, namely a shrinkage of 9.4% to 14.14 ± 0.02 mm, while parallel to the B-field the dimension increases (statistically) by 2.1% to 15.93 ± 0.04 mm. The lyophilized composite frozen without the B-field has a dimension of 14.77 ± 0.06 mm (94.7%) and 14.49 ± 0.23 mm (92.9%). The resulting cross-sectional area of the composite frozen with the B-field is 92.6%, and the composite frozen without the B-field is 87.9% of that of the mold cross section area.

Significant differences in the density of the freeze-cast magnetic composites were observed after lyophilization. The magnetic composite made with a slurry composed of 27% w/v Sendust flakes and 3% w/v Chitosan, results after lyophilization in a cell wall solid that, assuming it to be fully dense, is composed of 63.4% v/v Sendust flakes and 36.6% v/v Chitosan. Freeze casting introduces at the first level of the material's hierarchical architecture

an interlamellar porosity between the cell walls, and at the second level of the materials hierarchical architecture an additional porosity within the cell walls.

Table 1. Listed are the dimensions of the magnetic composite in the frozen and freeze-dried state.

	Dimensions (when frozen) [mm]	**Dimension (when freeze-dried) [mm]**		**Cross Section Area Percentage**
		Parallel to B-field	Perpendicular to B-field	
With B-Field	15.6 × 15.6	15.93 ± 0.04	14.14 ± 0.02	92.6%
Without B-Field	15.6 × 15.6	14.77 ± 0.06	14.49 ± 0.23	87.9%

The resulting density of the samples freeze-cast in the presence of the B-field was found to be ρ_{wB}^{*} = 0.354 ± 0.011 g/cm^3; the density of samples freeze cast without a B-field had a 21.5% smaller density of ρ_{woB}^{*} = 0.278 ± 0.024 g/cm.^{3} These values correspond to an overall porosity, *P*, of 94.3% and 95.6%, respectively, assuming a fully dense cell wall material of $\rho_{w,s}$ = 6.27 g/cm^3 calculated with a density, ρ, of solid chitosan of 1.31 g/cm^3 [40], and a density of the Sendust flakes (85% Fe, 9% Si, and 6% Al) of 6.82 g/cm^3.

2.1.2. Cell Wall Microstructure and Composite Architecture

A comparison of the SEM micrographs of magnetic-flake composites frozen in the presence and in the absence of an external magnetic field reveals that in both cases the cell walls are aligned parallel to the freezing direction (**Figure 2A-B**). Additionally, the cell walls are aligned parallel to the externally applied magnetic field in the sample frozen in the magnetic field, thereby forming the desired monodomain structure (Figure 2C-D, G). Noteworthy is also a difference in flake alignment within the cell walls. The flakes form a nacre-like structure with the flakes aligned parallel to the freezing direction in the case of the composites frozen in the

absence of a magnetic field. In contrast, the magnetic flakes align with their long axis with the magnetic field, but also rotate around the magnetic field direction. The outcome is a greater amount of porosity within the cell walls of the latter, in which chitosan bridges between individual flakes form an additional cellular structure, also within the cell wall composite (Figure 2E). The FIB-milled cross-sections of the cell walls (Figure 2F) highlight that the magnetic flakes line up mostly head to tail and rarely truly side by side. The flakes do not truly closely pack, particularly when self-assembled during freeze casting in the presence of a B-field.

2.1.3. Flake and Cell Wall Alignment into a Monodomain Structure

The volume renderings of the X-ray microtomograms of the magnetic-flake composites frozen in the presence and the absence of an external magnetic field confirm the observations made by SEM and FIB. **Figures 3A, B** illustrate the microstructure in the case of the composite frozen in the absence and in the presence of the magnetitic field, respectively. The chitosan phase is visible as more or less horizontal lines in the volume rendering of **Figure 4**, which is taken from the top 1-2 mm thick magnetic platelet depleted section in the composite frozen in a B-field. On most other sections the chitosan phase is hardly visible due to a combination of the small thickness of the structures that they form and, of course, their low X-ray absorption.

The structural characterization indicates that the samples frozen without a B-field (**Figure 5B**), have a honeycomb-like structure with a structure transverse to the freezing direction that may be considered isotropic, so that only two directions need to be distinguished: i) parallel to the freezing direction (||FD) and ii) perpendicular to the freezing direction (⊥FD). This is in contrast to the samples frozen in the presence of a B-field (Figure 5A), in which three orthotropic directions need to be distinguished: i) ||FD and perpendicular to the freezing direction ⊥FD both ii) parallel (⊥FD||BF) and iii) perpendicular to the B-field (⊥FD⊥BF).

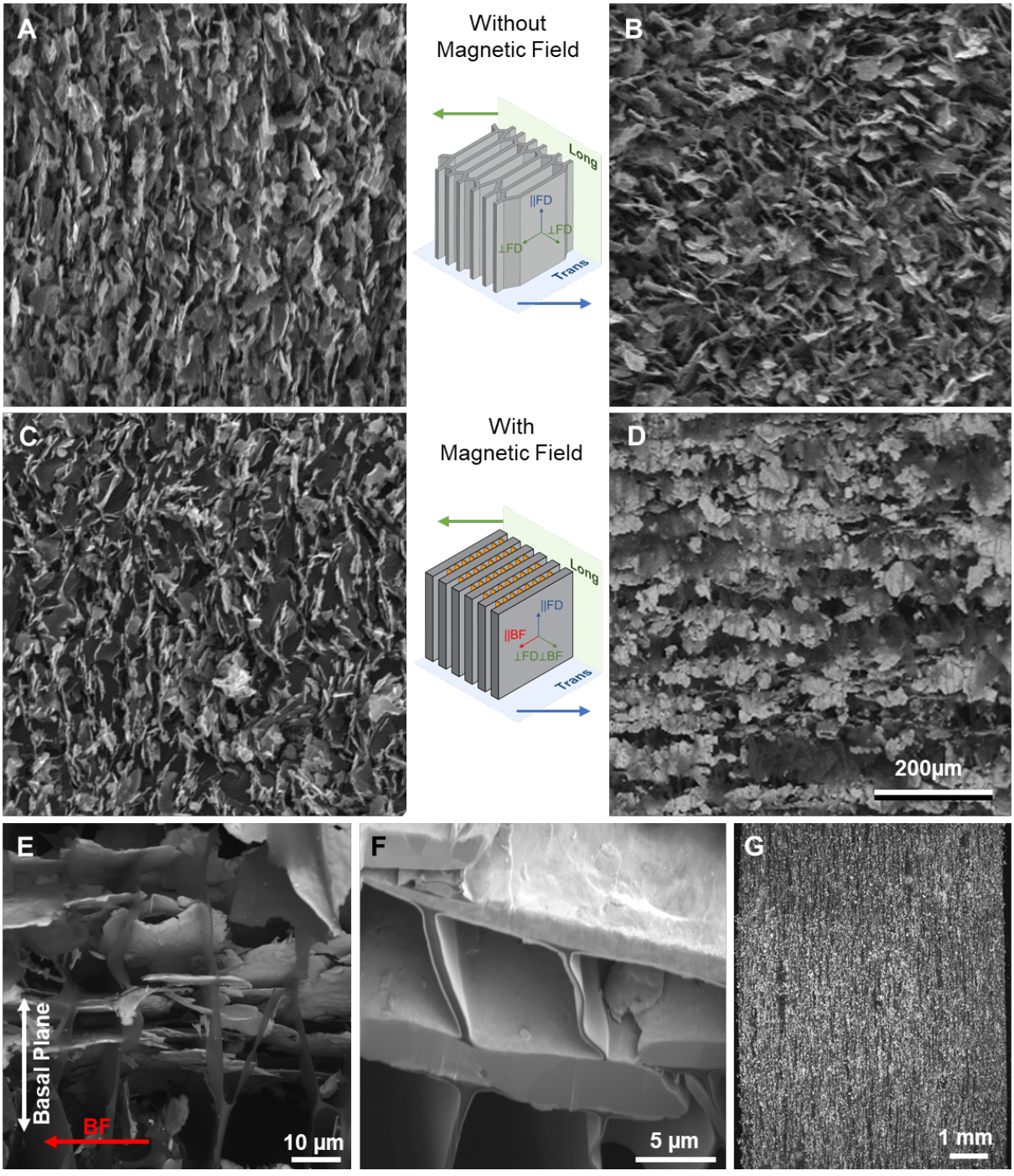

Figure 2. Scanning electron micrographs of longitudinal (A and C) and transverse (B and D) cross-sections of the magnetic composites frozen with and without an externally applied magnetic field. Images A to D share the scale bar shown in D. Scanning electron micrograph of the transverse cross-section in D, E, G imaged with back-scattered electrons, and (F) the FIB cross section of a cell wall of a magnetic composite frozen in the presence of a B-field.

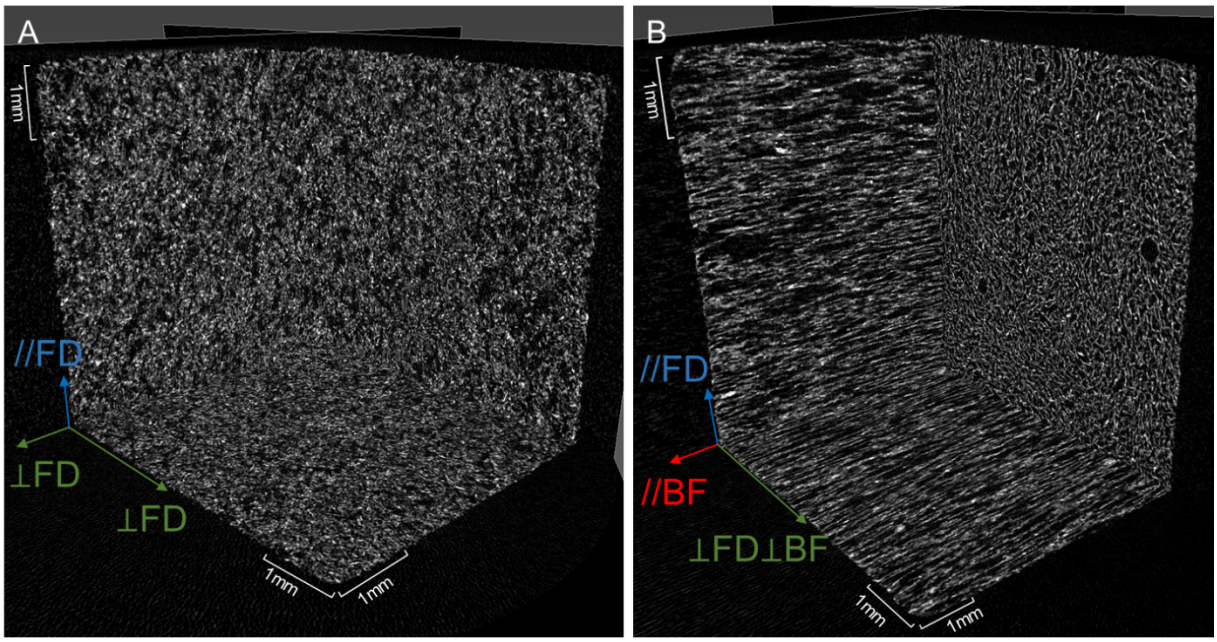

Figure 3. Orthogonal cross-sections (||FD, ||BF, and ⊥FD⊥BF) of the volume rendering of the magnetic composite (A) freeze-cast in the absence and (B) in the presence of a B-field.

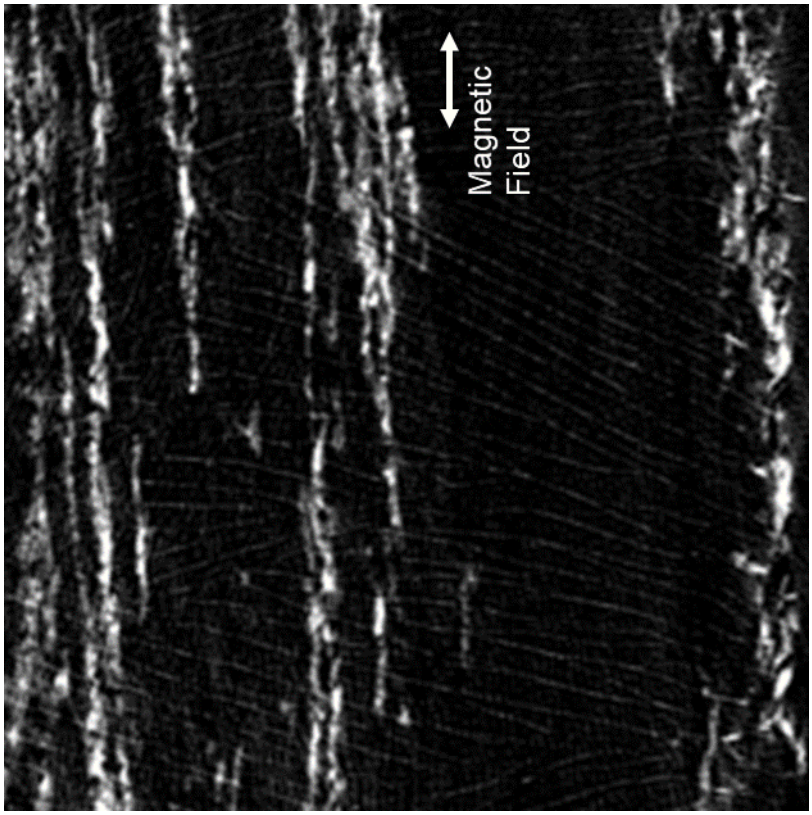

Figure 4. A transverse section through a volume rendering of a magnetic composite, freeze cast in the presence of a B-field, at a position close to the top of the magnetic fixture.

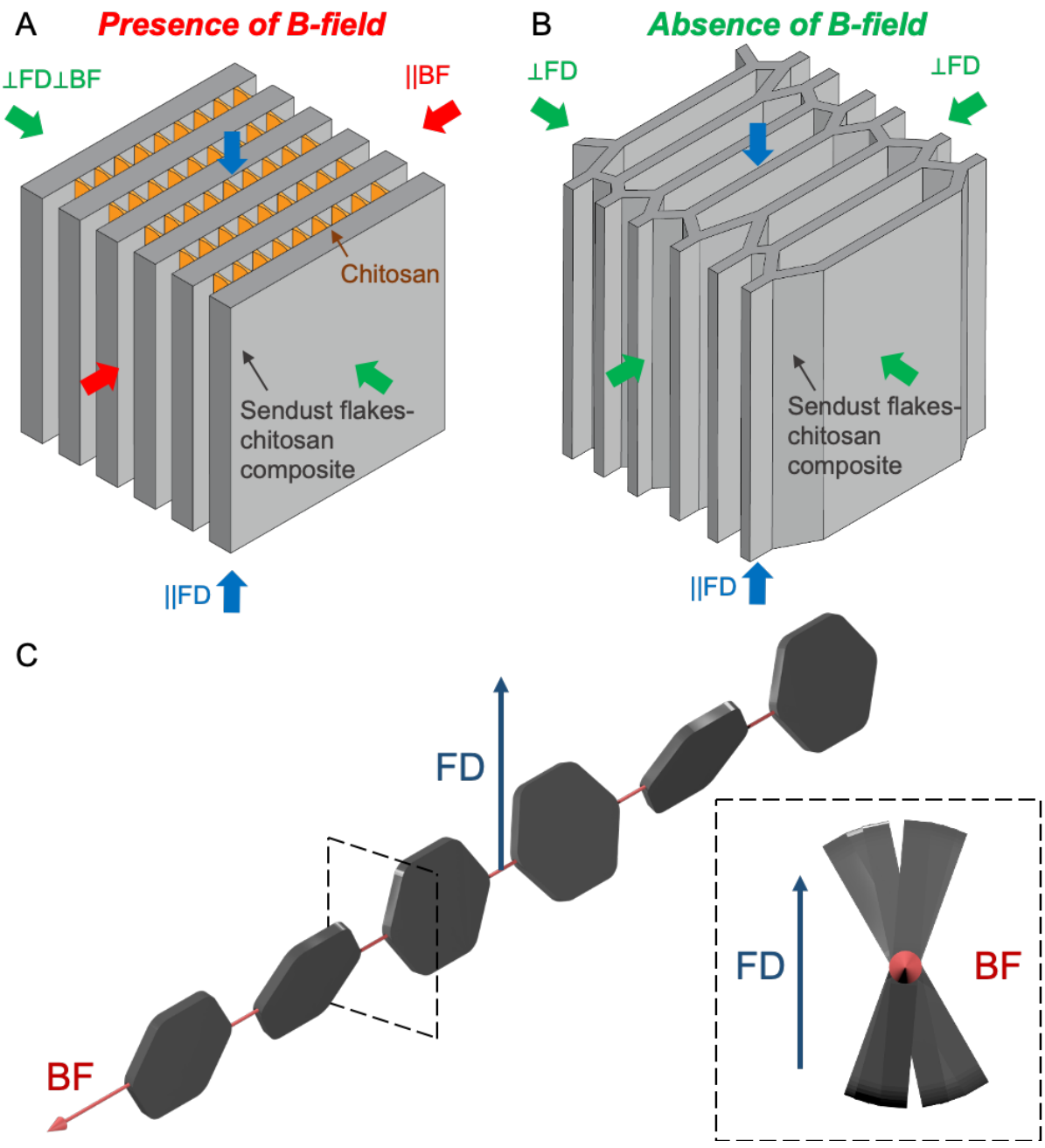

Figure 5. (A) Schematic of the monodomain structure of parallel aligned cell walls with nacre-like, magnetic-flake composite structure in the composite frozen with the B-field; (B) Schematic of the multidomain structure of the composite frozen without the B-field; (C) Schematic of possible flake rotations and alignments in the magnetic composites frozen in a magnetic field (A).

2.2. Mechanical Characterization

The results of the mechanical characterization of the magnetic composites are illustrated in **Figure 6** and summarized in **Table 2**. The insert in Figure 6 shows typical stress-strain curves for the magnetic-flake composites frozen in an externally applied B-field, tested ||FD and both ⊥FD ||BF) and ⊥FD ⊥BF. After a linear elastic region, the samples yield and exhibit a plateau region, during which the samples compact.

Table 2 lists modulus, yield strength, and toughness (work to 60% strain). The magnetic composite frozen in the presence of a B-field is stiffest and strongest in the ⊥FD||BF-direction with values twice as high as in the ||FD-direction, and four times as high as the values in the ⊥FD⊥BF-direction. The values for the modulus and the yield strength of samples frozen in the presence of a B-field are in the ||FD-direction about four times as high as those of the stiffest and strongest direction of the sample frozen without a B-field. In the ⊥FD-direction, the values for the modulus and the yield strength are about four and three times as high, respectively, as the ⊥FD⊥BF-direction of the samples frozen without the B-field.

The toughness (work to 60% strain) of the magnetic composite freeze cast in the presence of a B-field is highest perpendicular to the freezing direction and parallel to the B-field (⊥FD ||BF). In this direction it is about 20% higher than that parallel to the freezing direction (||FD) and about 80% higher than that perpendicular to both the freezing direction and the B-field (⊥FD⊥BF); it is also three times higher than the toughness perpendicular to the freezing direction of the sample freeze cast without an externally applied B-field. The toughness value in the tougher direction parallel to the freezing direction (||FD) of the sample frozen without a B-field is about the same as that of the least tough in the sample frozen in a B-field, it is also 66% higher than the toughness value perpendicular to the freezing direction (⊥FD).

Table 2. Mechanical properties (mean ± standard deviation) of the composite freeze cast with and without B-field determined in compression parallel to the freezing direction (||FD), the magnetic field (||BF), and perpendicular to the freezing direction (⊥FD, and when frozen without B-field) also perpendicular to both directions (⊥FD⊥BF).

Magnetic Composite	**Density ρ_{CM} [kg/m^3]**	**Relative Density $\rho_{rel,CM} = \rho_{CM}/\rho_{CM,s}$**	**Modulus [MPa]**	**Yield Strength [MPa]**	**Toughness [kJ/m^3]**
Frozen with B-Field	n = 3				
||FD	0.354 ± 0.011	5.7%	8.98 ± 1.79	0.47 ± 0.17	394.72 ± 70.84
||BF			20.42 ± 0.65	0.84 ± 0.12	471.35 ± 47.25
⊥FD ⊥BF			4.16 ± 0.35	0.21 ± 0.03	266.35 ± 39.51
Frozen without B-Field	n = 3				
||FD	0.278 ± 0.024	4.4%	4.95 ± 1.27	0.20 ± 0.01	279.58 ± 22.82
⊥FD			1.12 ± 0.11	0.07 ± 0.01	168.16 ± 10.77

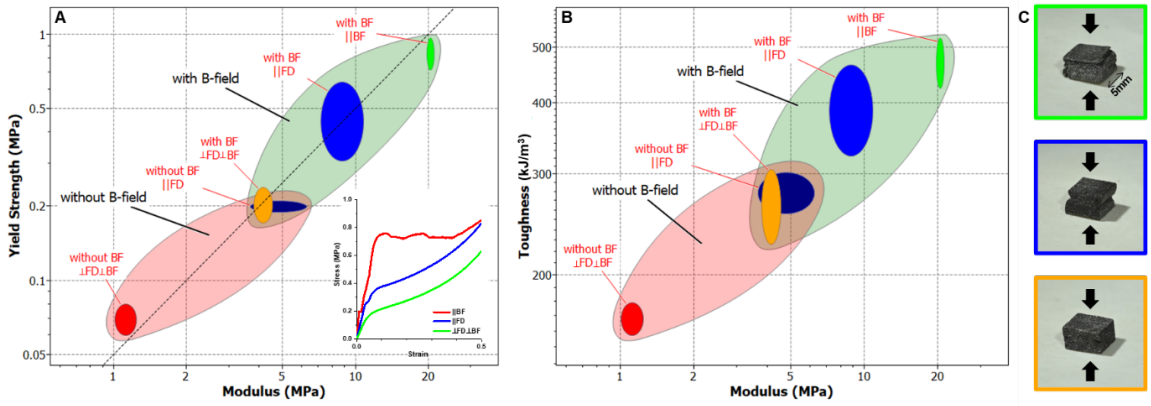

Figure 6. Property charts illustrate the correlation between (A) yield strength and modulus and (B) toughness and modulus. (C) The three photographs depict the samples after testing. The picture frames are color-coded to correspond to the stress-strain curves in (A) and the property bubbles in (A) and (B): the images in the green, blue, and orange frames show samples manufactured in the presence of a B-field after their having been compressed to 80% strain ||BF, ||FD, and ⊥FD⊥BF, respectively.

The property charts of Figure 6 illustrate the correlation between (A) yield strength and modulus and (B) toughness and modulus. The modulus to yield strength ratio of about 20 in all three directions is typical for porous or cellular materials [40]; the observed toughness reflects the degree of particle rotation and interlocking in the cell wall material in addition to preferential particle alignment.

2.3 A Magnetic Fixture for Uniform Magnetic Flux

In order to apply a uniform magnetic field to the slurry during freeze-casting, a custom-designed magnetic fixture composed of neodymium permanent magnets placed on the sides of the fixture with their north poles oriented in the same direction, and sandwiched between Si-steel laminations across the top and bottom of the stack was placed around the mold as shown in **Figure 7A**; Figure 7B shows the top view of the fixture topology (upper left). Finite element (FE) simulations of flux density for sample permeabilities, μ_r, of 1, 10, and 100, respectively, reveal that the magnetic fixture results in the desired uniform magnetic field between the top and bottom Si-steel plate laminations. Figure 7B illustrates that, as the sample permeability increases, more of the flux flows through the sample than the surrounding air, but that within the sample the flux remains uniform. Flux uniformity is so important, because we want the magnetic flakes to rotate into alignment with the field, but not translate their position. A nonuniform field would cause the flakes not only to rotate but also to move to regions of higher field concentration.

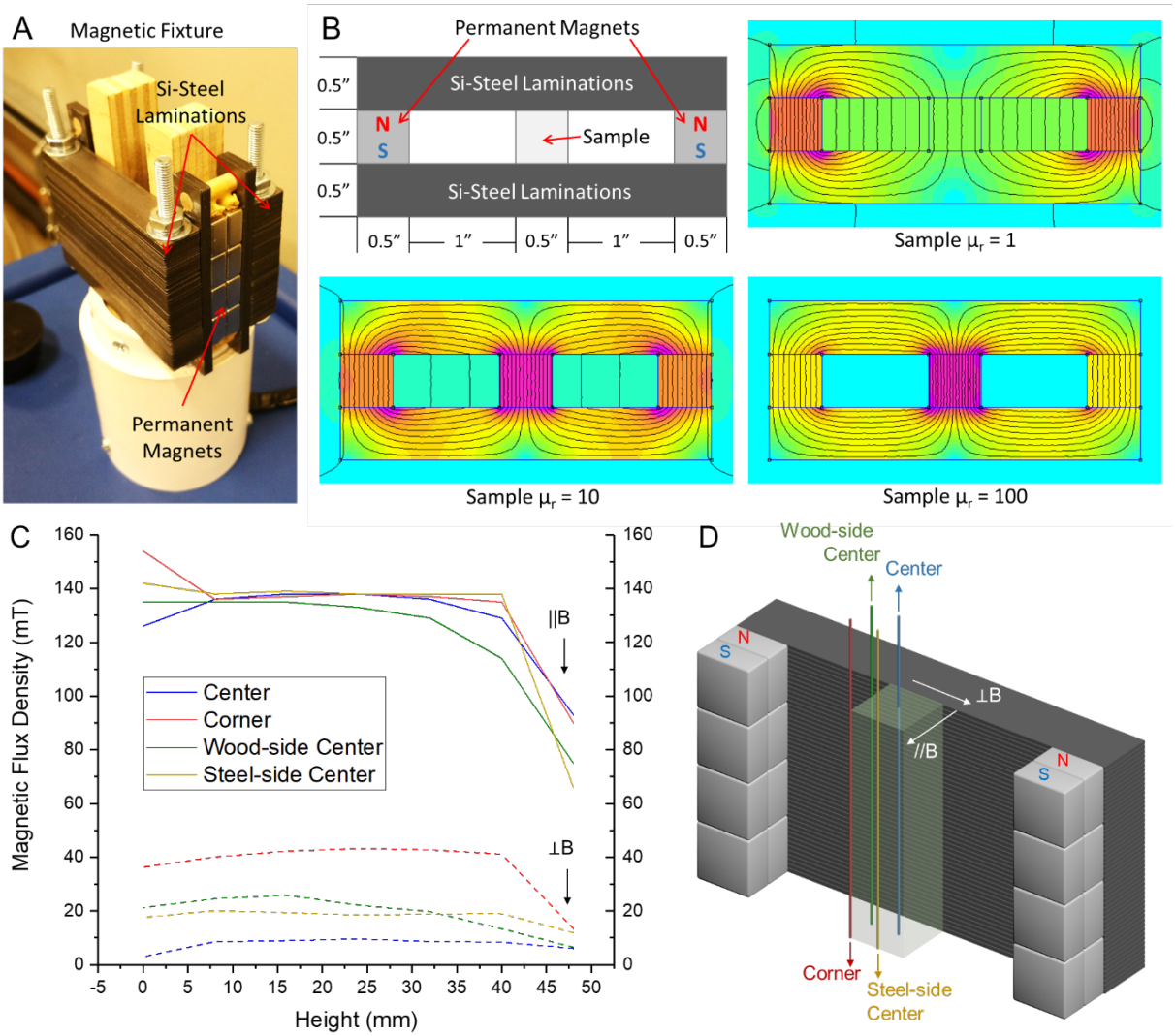

Figure 7. (A) Photograph of the magnetic freeze casting fixture; (B) Schematic of the magnetic fixture (top view) with finite element simulations for sample permeabilities, μ_r, of 1, 10, and 100 highlighting the uniform magnetic flux in the square sample in all cases. (C) Magnetic flux density within the magnetic fixture (D), measured with the probe aligned parallel (||B) and perpendicular (⊥B) to the applied B-field.

To verify the FE simulations, the magnetic flux densities at four different positions in the mold—center, corner, midpoint of steel lamination side, and wood side (Figure 7C,D) — were determined to be with values of 133.8 ± 4.6 mT, 139.5 ± 6.6 mT, 130.2 ± 7.5 mT, 138.8 ± 1.5 mT, respectively, almost constant for heights of 0-40 mm within the mold and up to 35 mm also across the mold. It decreased most for the measurements taken at the wood-side center of the mold starting at mold heights >35 mm.

2.4 Magnetic Performance Measurements

Permeability and quality factor were determined in the three orthogonal directions ||FD, ||BF, and ⊥FD⊥BF for both the samples frozen in the presence of a B-field and those frozen in the absence of a B-field, as well as for the PDMS-Sendust composite controls. Both PDMS and chitosan have much higher resistivity than the magnetic flakes, so the different binders were expected to have no significant effect on the measured power loss. **Figure 8-11** illustrate the respective real and imaginary parts of the permeability and the quality factors determined. The results for the freeze-cast magnetic composites (Figure 9 and 10) reveal also in the magnetic performance the considerable anisotropy, first observed in the structural, then also in the mechanical performance, of the freeze-cast composites.

Figure 8A shows the real, μ_r', and the imaginary, μ_r", parts of the permeability, and Figure 8B the quality factor, Q, for frequencies from 10 kHz to 1 MHz for the Sendust-PDMS composite with randomly oriented magnetic flakes. The "Ref" traces are measurements of the toroid, and the "A", "B", and "C" traces are measurements of the cubic reference core, illustrating the isotropy of the samples in comparison. Figure 9A and 9B show the results obtained for the Sendust-PDMS composite prepared with a B-field applied during cross-linking, in which the magnetic flakes are aligned parallel to the direction marked "A"; they reveal that the permeabilities in the B and C directions increase, while that in the A direction decreases. The results for the magnetic composites, freeze-cast in the absence (Figure 10) and in the presence (Figure 11) of a B-field, reveal that the real part of the permeability stays within a range of 4-6 for samples freeze cast without B-field and within a range of 4-7 for samples freeze cast with an applied B-field. For both sample types the quality factor improved with respect to the reference sample in at least two directions.

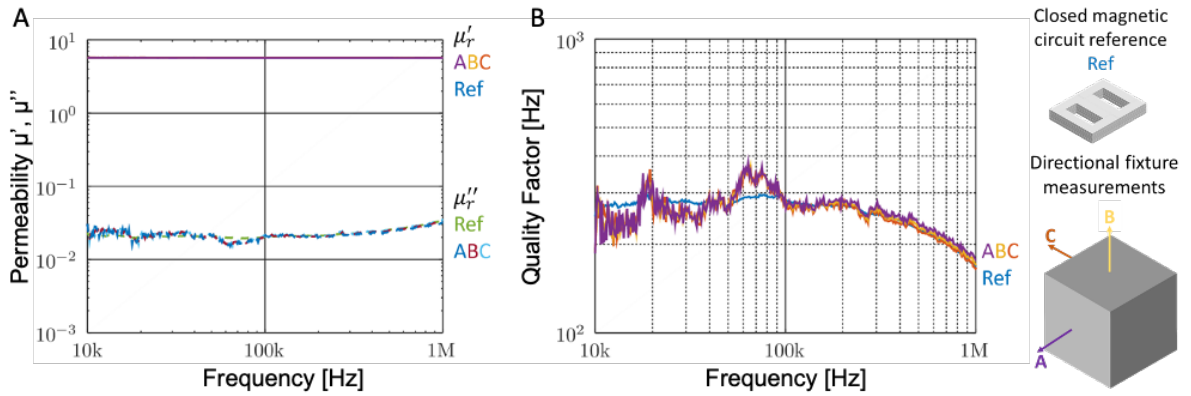

Figure 8. A) Permeability and B) quality factor of randomly oriented Sendust-flake-PDMS composite are reflected in a magnetic/electric performance that is similar in the three orthogonal directions.

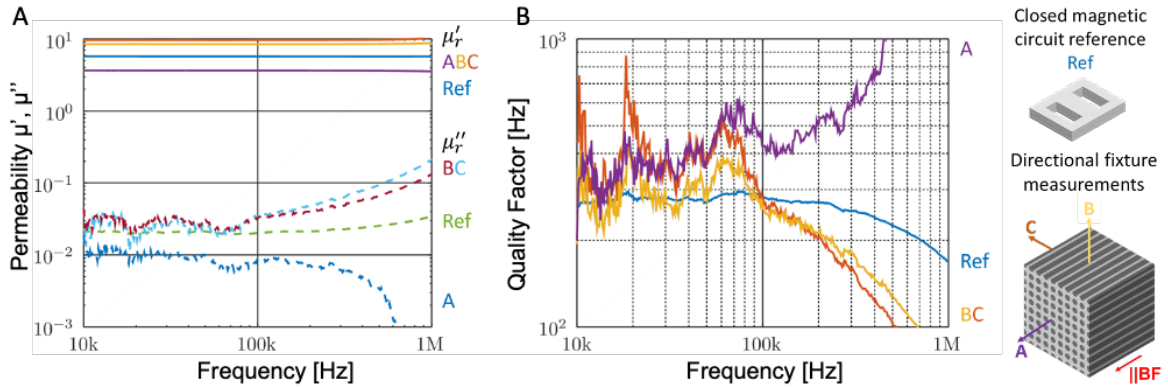

Figure 9. A) Permeability and B) quality factor of the magnetically aligned Sendust-flake-PDMS composite. “A” in Figure B) indicates the sample orientation in which the majority of flakes are aligned parallel to the B-field. “B” and “C” indicate the two directions perpendicular to the flake alignment.

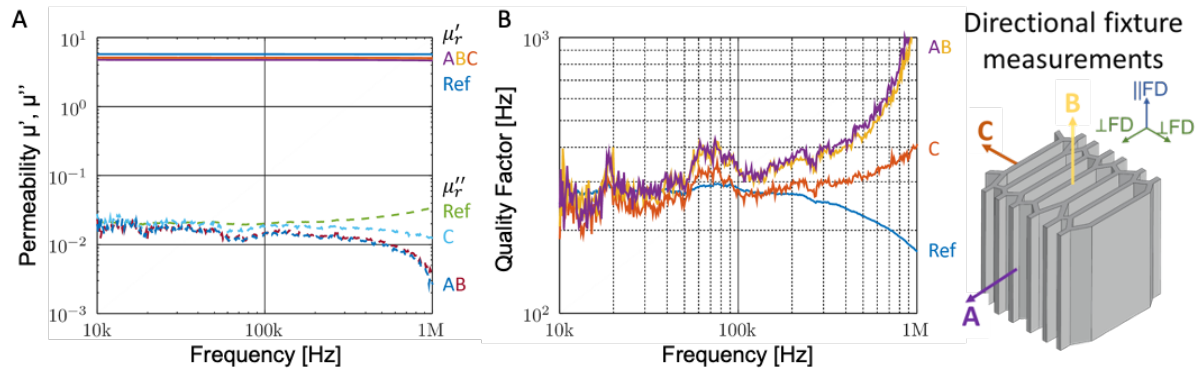

Figure 10. A) Permeability and B) quality factor of the Sendust-flake composite freeze cast without B-field. “A” and “B” in Figure B) indicate the directions, in which the majority of the flakes are aligned, in this case, with the cell walls formed parallel to the direction of solidification and parallel to the cell walls in one domain. “C” indicates the direction perpendicular to the flake and cell wall alignment.

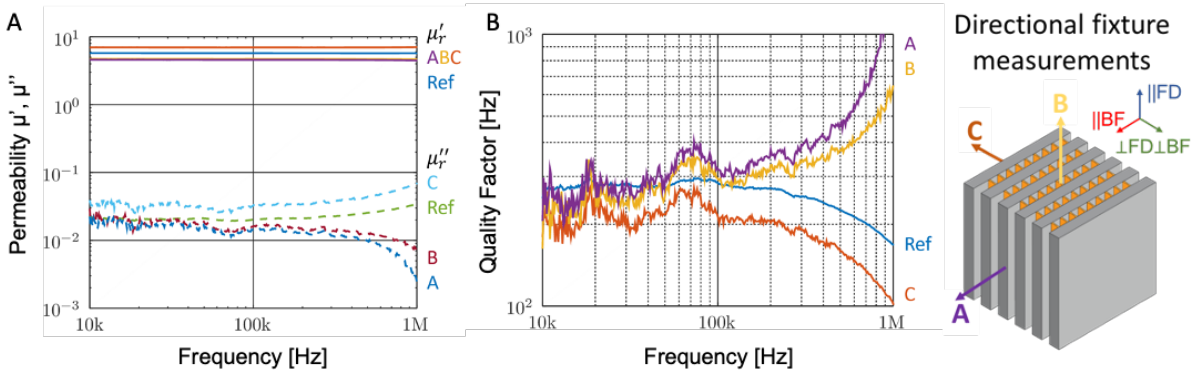

Figure 11. A) Permeabiliy and B) quality factor of the Sendust-flake composite freeze cast in the presence of a B-field. “A” and “B” indicate directions in which the majority of flakes is aligned. “A” indicates the direction parallel to the B-field during freeze-casting, with best alignment of flakes and cell walls, “B” parallels the direction of the second-best flake and cell wall alignment, the direction of solidification. “C” indicates the direction perpendicular to the flake and cell wall alignment.

3. Discussion

3.1. Magnetic Composite Structure

3.1.1 Effect of Processing on Density and Volume Fractions

The about 27% higher density (0.354 ± 0.011 g/cm3) of the magnetic composite freeze cast in the presence of a B-field in comparison to the density (0.278 ± 0.024 g/cm3) of the composite freeze cast in the absence of a B-field results from several effects that reinforce each other. Of particular importance is that the presence of the B-field prevents sedimentation and thereby maintains a homogeneous distribution of the magnetic flakes in the slurry, which due

to their size and material density are otherwise prevented from sedimentation only by the high viscosity chitosan binder and due to increasing mechanical particle interlocking.

Flake sedimentation in the absence of a B-field field depends on three competing forces, gravity:

$$F_g = gm \tag{1}$$

where g = 9.81 m/s^2 is the gravitational constant and *m* is the particle pass,

and the drag or frictional force counteracting it:

$$F_d = 6\pi r\eta v_F \tag{2}$$

where r is the effective radius of the oblate ellipsoid calculated from its and flake thickness and diameter values of a = 1 µm and b = 25µm, respectively as:[41]

$$r = 0.707\, b\left(\frac{3a}{2b} * \arctan\frac{b}{a}\right)^{0.5} = 1.623\ \mu m \tag{3}$$

and η is the viscosity of the solvent, and v_F is the flow velocity relative to the flake,

and, finally, the buoyancy force, which also counteracts gravity:

$$F_b = \rho_L g V_F = \rho_L g 2\pi b^2 a \tag{4}$$

where ρ_L is the density of the liquid, here the chitosan solvent, and V_F is the flake volume.

The balance of these forces:

$$F_s = (\rho_P - \rho_L)2\pi b^2 ag - 6\pi r\eta v_F \tag{5}$$

determines the speed of sedimentation of the flake (neglecting particle-particle interactions, shear flow, etc.):

$$v_F = \frac{(\rho_P - \rho_L)2\pi b^2 ag}{6\pi r\eta} = 33.147\ \mu m/s \tag{6}$$

with Sendust flake material and the chitosan solvent densities of ρ_F = 6.82 g/mL and ρ_L = 1.01 g/mL, a chitosan solution viscosity of η = 300 mPa.s, and a flake volume of

V_F = 1963.5 μm^3 the flakes sediment at a speed of 120 mm per hour. Considering that it takes 20 min to solidify the entire sample at an applied cooling rate of 10°C/min, flake sedimentation is a factor that contributes significantly to structure formation and needs to be minimized.

The structural characterization of the Sendust flakes showed that a large fraction of them have a diameter smaller than 50 μm, which sediment at a much lower velocity, because sample volume scales with the square of the particle radius. Additionally, mechanical interactions and interlocking of the flakes contribute significantly to the flakes' mobility, so that also in the absence of a B-field sedimentation is slower than estimated by the above. Similarly, the increasing height of already solidified material decreases the distance, over which sedimentation can actually occur.

Thus a more homogeneous magnetic flakes distribution along the height, as well as higher magnetic flake loading can be achieved by freeze casting the presence of a B-field, in comparison to freeze casting in the absence of B-field, making magnetic freeze casting the more efficient process.

Finally, a smaller contribution to differences in material density is due to differences in composite shrinkage during freeze drying, when the polymeric phase contracts due to moisture losses. The shrinkage depends on the distribution of the chitosan phase, both within the cell wall material and within the lamellar structure that the cell walls form. Pure chitosan structures, such as those between the cell walls, can contract more than those of the Sendust-chitosan composite cell walls. Similarly, a higher composite cell wall density with greater order in assembly and more closely packed flakes prevents material contraction and thereby reduces composite shrinkage.

3.1.2. Flake and Cell Wall Alignment into a Monodomain Structure

The structural analysis by SEM, FIB, and X-ray microtomography revealed that in the

samples frozen without a magnetic field, the Sendust flakes self-assemble into a nacre-like cell wall structure similar to the one observed for alumina flakes [23]. In the absence of forces other than those of the shear flow between the ice dendrites, a multi-domain structure typical for freeze-cast materials results, with preferential alignment along the freezing direction (Figure 3B).

When a weak magnetic field is applied during freeze casting, water, a diamagnetic material of small magnetic susceptibility (estimated to be $\chi = -1.631\times10^{-10}$ m^3/mol [42]) is only minimally affected [43]. However, we observe a smaller, more stunted pore size as defined by the chitosan cells walls. In contrast, the Sendust flakes experience either a torque in a uniform B-field, or both a torque, T_m, and a translational force, F_m, in a non-uniform B-field. The torque exerted on a flake, approximated by an oblate ellipsoid, can be estimated to be [25]:

$$\overrightarrow{T_m} = -\frac{dU_m}{d\theta} = \frac{2\pi ab^2}{3}\frac{\bar{\chi}^2}{\bar{\chi}+1}\mu_0 H^2 \sin 2\theta \qquad (7)$$

where a and b are the short and long radii of the oblate ellipsoid, $\bar{\chi}$ is the shape corrected susceptibility $\bar{\chi} = 3\chi/(\chi+3)$ [25], χ is the susceptibility of the material, H is the magnetic field strength [A·m^{-1}], $\mu_0 = 4\pi\times10^{-7}$ N·A^{-2} is the magnetic permeability of free space, and θ is the angle between the long flake axis and the magnetic field direction.

With an estimated susceptibility of χ = 100,000 m^3/mol for the Sendust material, a magnetic field strength of H = 1.1 × 10^5 A·m^{-1}, and flake thickness and diameter values of a = 1 μm and b = 25 μm, respectively, and assuming a flake misalignment with the magnetic field of θ = 45°, at which the torque reaches its maximum, we calculate the flake to experience a magnetic torque of $T_m = 4.5\times10^{-11}$ N·m, which agrees well with the previous studies [25]. The true torque on the magnetic flake will be lower than this value, due to magnetic induction and resulting particle-particle and particle-liquid interactions.

Because the external B-field induces magnetization in the Sendust flakes, each magnetic

flake experiences both the uniform external magnetic field, which causes the flakes to rotate and to preferentially align with the field, and the non-uniform B-fields of neighboring flakes, which cause the flakes to form head to tail flake chains (Figure 5C). A second effect of the non-uniform induced magnetization is that, laterally, the particles are forced apart, so that a truly nacre-like close packing such as that observed with alumina platelets [23] cannot be achieved with magnetic flakes and a significant cell-wall porosity results. This effect is enhanced by mechanical particle-particle interaction that result from the particle rotation, and their interlocking.

Finally, because the magnetic field forces are greater than those of the shear flow, which would otherwise align the flakes and promote their self-assembly into a close-packed nacre-like structure, the particles can rotate around the field lines and are held by the stronger forces of the magnetic field in this rotated position. As a result, the cell walls are undulated and not as straight and well-aligned with the freezing direction as those of the samples freeze cast in the absence of the B-field. The effect of the magnetic forces became particularly obvious in the top part of the sample, which protrudes out of the uniform B-field section of the mold; in this region, the magnetic flakes were pulled down into the B-field, leaving behind a flake-depleted slurry (Figure 4) that resulted in a predominantly polymeric scaffold section outside of it.

3.2. Mechanical Properties and Performance

Compression tests were performed, not only to determine the mechanical properties of the magnetic composites, but also to analyze the progression of failure and mode of compaction, which is of importance for possible applications such as inductor or transformer cores. Typical stress–strain curves are shown in Figure 6. The values for the Young's modulus were calculated from the slope of the initial linear region. The yield strength was taken to be the peak stress before compaction, when a yield point existed, or determined from the point of intersection between the tangent line to the elastic region and the tangent line of the plateau, or collapse

region, in the absence of a yield point. The toughness was calculated from the area underneath the compression curve up to a strain of 60%. The stress–strain curves of Figure 6 illustrate that the freeze-cast magnetic composites behave like a typical cellular solid.

According to the Gibson-Ashby model of cellular solids, three structural features determine their mechanical and physical properties: (i) the composite's relative density, (ii) the pore morphology, which results from the ice templating and the externally applied magnetic field, where applicable; and (iii) the properties of the solid that forms the cell wall solid. [40,44]

The mechanical properties stiffness, E, and strength, σ, of cellular solids scale with their relative density, $\rho_{rel} = (\rho^*/\rho_s)$, as:

$$E^* \propto E_s \ (\rho_{rel})^n \tag{8}$$

and

$$\sigma^* \propto \sigma_s \ (\rho_{rel})^m \tag{9}$$

with $n_1 = 2$ and $m_1 = 1.5$ for equiaxed foams, and $n_2 = m_2 = 1$ for honeycombs.

In our case of the magnetic composite, the relative density $\rho_{rel,MC}^* = \rho_{MC}^*/\rho_{W,s}$ is defined by the density of the freeze-cast composite ρ_{MC}^* is and the density, $\rho_{W,s}$, of the solid from which the cell walls are formed; the overall porosity of the magnetic composite is defined as $P = 1 - \rho_{rel,MC}^* = 1 - \rho^*/\rho_{W,s}$. In analogy, the relative density of the cell walls, $\rho_{rel,W}^* = \rho_W^*/\rho_s$ is defined by the density of the porous cell wall, ρ_{MC}^* , and the density, ρ_s , of the fully dense solid from which the cell walls are formed; the overall porosity of the cell wall is defined as $P_W = 1 - \rho_{rel,W}^* = 1 - \rho^*/\rho_{W,s}$. The mesoporosity contained between the cell walls, $P_m = P - P_W$, is the difference between the overall and the cell wall porosity; the corresponding relative density of the mesoporous material can be calculated from the ratio of the density of the magnetic composite to that of the effective density of the cell wall material, $\rho_{rel,m}^* = \rho_{MC}^*/\rho_W^*$.

Differences in pore morphology are cause for the significant differences between the mechanical properties of composites frozen in the presence and absence of the magnetic field illustrate this: both composite types have the same composition and a very similar relative density, but differ significantly in their lamellar architecture, and cell wall microstructure. Performance defining are the shape and orientation of the cell walls and the amount of mesoporosity formed between them as well as the flake orientation and resulting microporosity within the cell walls, the latter determining the cell wall material properties. All of these structural features define the mechanical properties and failure modes, the ease with which the initially porous material can be compacted as well as the structure and performance of the compact, and in parallel also their magnetic performance.

A brief comparison of the experimentally determined mechanical property values with those estimated on the basis of the Gibson-Ashby model-based reveals whether the properties of the magnetic composites fall within the expected range. The mechanical properties of the magnetic composite can be estimated in a three-step analysis of its hierarchical structure (**Figure 12**); it takes into consideration the cell wall's composite structure and both the composite's mesoporosity contained between the cell walls, and the microporosity within the cell walls [23].

First, we estimate a lower bound modulus value, $E_{W,s}$, of the cell wall solid (Figure 12) based on the Reuss model:

$$E_{w,s} = \frac{\sigma}{\varepsilon_{w,s}} = \frac{E_{Chi}E_{SD}}{VE_{Chi} + (1-V)E_{SD}} \tag{10}$$

with a literature value for the modulus of Sendust of E_{SD} = 300 GPa [45] and an experimentally determined (in tension at 35% r.h.) modulus of chitosan of E_{Chi} = 3.7 GPa [46].

With a Sendust volume fraction of 63.4%, we calculate the modulus of the cell wall solid to be $E_{W,s}$ = 9.9 GPa. In the second step, for the second level of the hierarchy (Figure 14),

we first calculate the density of the porous cell wall materials, ρ_W^*, of the cell wall material from its porosity, $P_{W,woB}$ = 30% (frozen without B-field) and $P_{W,wB}$ = 40% (with B-field), estimated by image analysis of the SEM micrographs and the XMT tomograms [40,44]:

$$\rho_W^* = \rho_{W,s}\,(1 - P_W) \tag{11}$$

where $\rho_{W,s}$ = 6.27 mg m^{-3} is the density of the fully dense cell wall composite material.

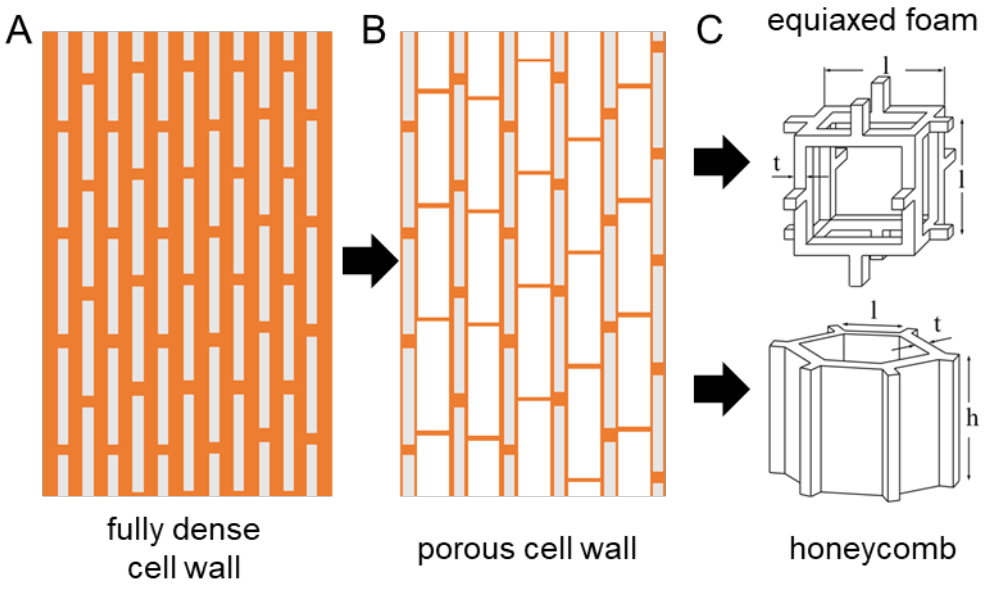

Figure 12. Schematic of hierarchical structure, porosity, and properties. (A) First level: the composite material solid of which the porous cell walls are composed. (B) Second level: the porous cell wall with a foam-like pore structure, that forms the cellular solid of the freeze cast magnetic composite. (C) Foam-like (lower bound) and honeycomb-like (upper bound) pore structure of the freeze-cast magnetic composite. Figures adapted from [47].

Then, applying the Gibson-Ashby model for an equiaxed foam [40,44] we can calculate the modulus of the porous cell wall material:

$$E_W^* \propto E_{W,s}\left(\frac{\rho_W^*}{\rho_{W,s}}\right)^2 \tag{12}$$

to be 3.56 and 4.85 GPa for samples frozen with and without a B-field respectively (**Table 3**).

The relative density of the magnetic composite as a function of mesoporosity only is calculated as:

$$\rho_{rel,m}{}^{*} = \frac{\rho^{*}_{MC}}{\rho^{*}_{W}} \quad (13)$$

to be 0.354/3.76 = 9.41% and 0.278/4.39 = 6.33%, thereby subtracting from the overall porosity the porosity contained in the cell wall material. With Equation 8 and 9, we can estimate the modulus of the freeze-cast magnetic composite for both the upper bound of a honeycomb-like and the lower bound of a equiaxed foam structure to be 335.4 MPa and 31.6 MPa for the samples frozen in the presence and 307.3 MPa and 19.5 MPa for the samples frozen in the absence of the B-field (**Table 4**).

Repeating the property estimation for the magnetic composite scaffold strength, assuming the properties and correlations listed in Table 3, a similarly good agreement with the Gibson-Ashby model results (Table 4).

Plots of relative modulus ($\frac{E^{*}_{MC}}{E^{*}_{W}}$) and relative strength ($\frac{\sigma^{*}_{MC}}{\sigma^{*}_{W}}$) against relative density ($\frac{\rho^{*}_{MC}}{\rho^{*}_{W}}$), thus normalizing each magnetic composite property with the property of the porous cell wall material, are shown in **Figures 13 A and C**, respectively. The relative modulus of the freeze cast magnetic composite falls into a similar range as that reported before for nacre-like freeze cast alumina composites [23], even though the magnetic composite has a porous cell wall and the alumina composite truly has a nacre-like, dense and close-packed cell wall.

Several reasons could lead to this result. The magnetic flakes are well aligned in the presence of a B-field, which leads to a delay of cell wall bending and buckling in compression, even if the flakes are not as closely packed as the alumina platelets in the composite's ceramic counterpart. The well aligned cell walls generated by the magnetic field as well as the chitosan bridges that form pillar-like supports for the cell walls, enhance the mechanical perform of the Sendust-chitosan composite in a similar fashion as previously reported for alumina composites with a nacre-like structure [23,47], in that case generated by freeze casting in the absence of magnetic field. Comparing our freeze-cast magnetic flake composites with surface-magnetized

flake-based materials that were first freeze cast in a magnetic field and then sintered [11,13,16,18], we note a superior property enhancement of a factor of 4 in both modulus and strength.

Table 3. Properties of the cell wall material.

	Volume Fractions in Cell Wall Solid (theoretical) [%]	**Density of Cell Wall [mg/m³]**	**Relative Density of Freeze-Cast Composite** $\rho_{rel,MC}$* [%]	**Relative Density of Cell Wall** $\rho_{rel,w}$* [%]	**Modulus [GPa]**	**Strength [MPa]**
Sendust	100	6.82			300[45]	540 (bending)
Chitosan	100	1.31			3.7[46]	64 (tension)
					Reuss	
Sendust-Chitosan Composite (fully dense, estimate)	63.4 (Sendust) 36.6 (Chitosan)	$\rho_{w,s}$ = 6.27			$E_{W,s}$ = 9.9 (Reuss)	$\sigma_{W,s}$ = 23.4 (lower bound)
Frozen with B-field					**Gibson-Ashby**	
Sendust-Chitosan Composite (porous, estimate)	38.0 (Sendust) 22.0 (Chitosan) 40% Air	ρ_W* = 3.76	5.65	60	E_W* = 3.56	σ_W* = 10.88
Frozen without B-field						
Sendust-Chitosan Composite (porous, estimate)	44.4 (Sendust) 25.6 (Chitosan) 30% Air (without BF)	ρ_W* = 4.39 (without BF)	4.43	70	E_W* = 4.85	σ_W* = 13.70

Table 4. Properties of the magnetic composites freeze cast with and without a B-field.

	Relative Density of Composite with Porous Cell Walls (%) $\rho_{rel,MC}^{*}$	**Modulus (Equiaxed Foam) [MPa]**	**Modulus (Honeycomb) [MPa]**	**Strength (Equiaxed Foam) [MPa]**	**Strength (Honeycomb) [MPa]**
Frozen with B-Field (theory)	9.41	31.6	335.4	0.314	1.023
Frozen with B-Field (exp.)		4.16 - 20.42		0.21-0.84	
Frozen without B-Field (theory)	6.33	19.5	307.3	0.218	0.868
Frozen without B-Field (exp.)		1.12-4.95		0.07-0.20	

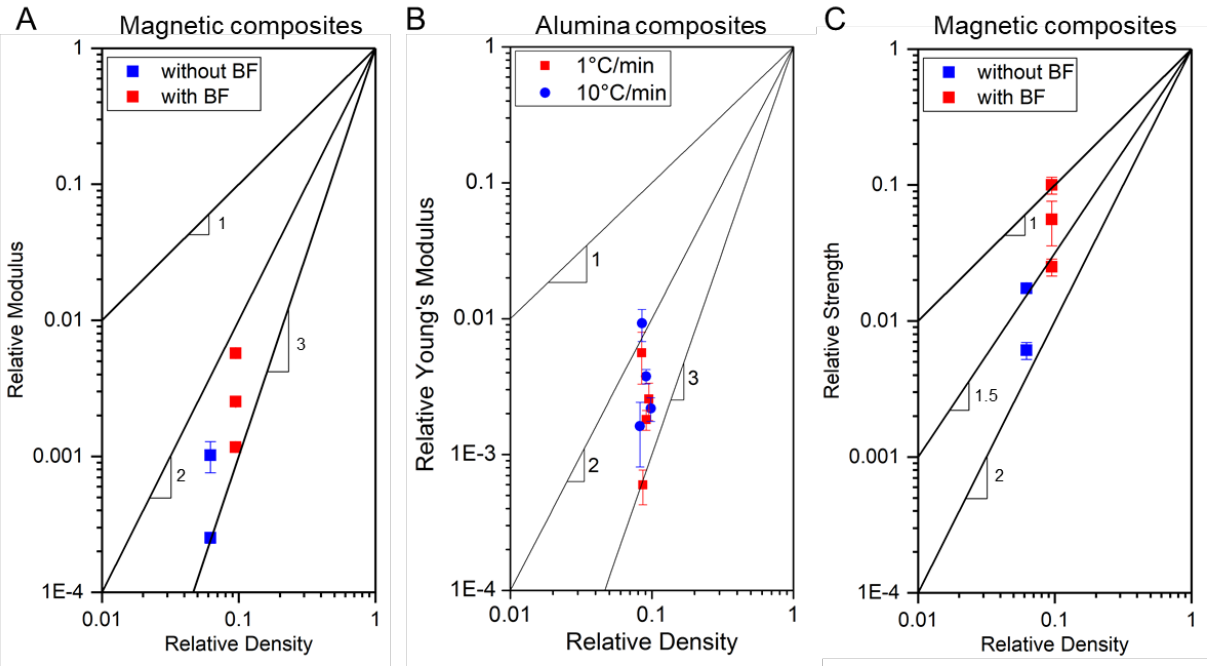

Figure 13 (A) Relative modulus of the magnetic composites plotted against relative density of the composite. The moduli of both types (frozen in the presence and in the absence of a B-field) fall between lines of slope 2 and 3. B) Relative modulus plotted against relative density for nacre-like freeze cast alumina scaffolds.[47] Figure adapted from [47]. (C) Relative strength plotted against relative density for the magnetic composites. The strengths of both types fall between lines of slope 2 and 1.

The significant differences in mechanical properties and performance reflect the differences in cell wall alignment, on the one hand, and the magnetic flake alignment in the cell walls, on the other. After the initially linear region of the stress-strain curve, in which the cell walls are loaded in compression and lower than ideal property values can be explained by cell wall imperfections and misalignments, the sample yields, when strain localization causes a region to buckle. Following the yield point, damage extends through the sample, progressively folding and collapsing in a concertina-like fashion. In the case of samples compressed perpendicular to the freezing direction and parallel to the B-field ($\perp$FD ||BF), compaction occurs at relatively constant stress, in the other two directions the stress increases with increasing strain.

Rupture and fracture near the surface of the samples occurred only in materials freeze cast in the presence of a B-filed when tested ⊥FD ||BF samples and only at a higher compression strains, likely because of the higher flake to chitosan ratio and a resulting higher cell wall stiffness and strength. In the (⊥FD ⊥BF) direction sample compaction is particularly smooth and regular, likely because the cell walls and the flakes within the cell walls are initially, and to a larger extent than in the other directions, spaced and supported by polymer cell walls and bridges.

3.3. Preliminary Magnetic Performance Measurements

Magnetic flake composites have low eddy current loss only if the flux is oriented along the long dimensions of the flakes (as opposed to through their face). Thus, in order to properly optimize the magnetic composite by optimizing the fabrication process, a method of accurately measuring the power loss in each direction of flux orientation is essential. Core loss is typically measured on a closed magnetic circuit, which is an ideal arrangement, if the material can be easily formed into a closed shape, such as a toroid, and it has low power loss in the two directions of the flux path. However, these conditions are not always met and a rod or bar core sample must be used.

Forcing the magnetic field within a magnetic core sample into only one direction could be accomplished with a high permeability return path as long as the power loss of the return path is significantly lower than the material tested. However, if the return path loss is on the same order as the test sample loss, then separating the two loss mechanisms becomes very difficult due to the nonlinear nature of the core losses. Since the goal of this study is to produce materials that will have power losses lower than typical high permeability materials, the magnetic return path is not a viable option. Therefore, the open magnetic circuit characterization method and a custom-designed magnetic impedance analyzer test fixture

(**Figure 14)** were used, so that the parasitic loss mechanisms could be removed from the measurement.

The three traces of the Sendust-PDMS reference sample with randomly oriented flakes are nearly identical to the toroid measurement, indicating that the sample is isotropic. These results obtained for the Sendust PDMS reference sample prepared in a B-field illustrate that a magnetic alignment of the Sendust flakes is possible and that the alignment results in the desired increased quality factor in one direction of flux.

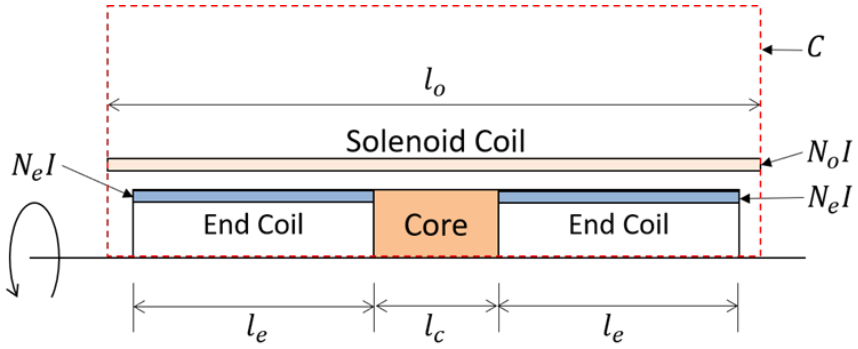

Figure 14. Definitions of variables used to develop an approximate analytical expression of the measurement fixture behavior: l_o is the total length of the outer solenoid coil of N_o turns, in which two end coils of the N_e turns and a length of l_e, and the tested core of length l_c are contained. The same current, I, is used for all coils during the measurement.

In the case the of samples frozen without a B-field (Figure 10), direction "A" parallels the freezing direction and direction "B" parallels the majority of the cell walls. Both are the best performing ones, because in these directions, the flakes are alignment with their thin dimension, which results in the smallest area of the eddy current loop, thus the smallest losses. In contrast, the large flake dimension is exposed in the "C"-direction, which results in a comparatively large eddy loop and thus a much lower quality factor. The presence of short, curved cell wall sections that effectively bridge the lamellae in this composite give rise to the slightly improved performance in the "C"-direction in comparison the sample frozen with a B-field present.

In the case the of samples frozen with a B-field (Figure 11), direction “A” parallels the B-field direction during freeze casting, and “B” parallels the freezing direction. The flake rotation around the B-field in the freezing direction is the cause for the exposure of a slightly larger cross-sectional area and thus a larger eddy current loop and losses in the “B”-direction. This small flake rotation also results in a slightly improved performance in the “C”-direction, because it leads to a small reduction in the eddy current loop area and loss.

Of particular importance for the composite’s excellent magnetic performance and also its mechanical performance is that magnetic composites freeze cast in a B-field have a monodomain structure, in which the cell walls of the entire sample are aligned. The reason for our observing a very similar performance in the “A” and “B” directions of the magnetic composite frozen without the B-field is likely that the cube specimen was cut from a single domain, thus with a preferential cell wall alignment. In this case, the flakes are aligned in two dimensions in the plane defined by the cell wall. Since this observation applies also when the freeze casting is performed without the B-field, a similarly good performances in the “A” directions is observed for the two types of the freeze-cast magnetic composite. The slightly better magnetic performance in the B-direction of the magnetic composite frozen without a B-field, in comparison to the one frozen in the presence of a B-field, is due to the more significant effect of flake rotation (Figure 5C). The sample frozen without a B-field could have the long axis of the pore parallel to the B direction (Figure 5A), then the contribution of eddy current from the long side of the cell wall is limited, taken advantage of the two dimensional alignment of the flakes in the cell wall. The major contributor of the eddy current is the cell wall on the short axis (Figure 5B), which might not be as significant as the rotating flakes.

While this material is well suited for use with a high permeability material in the flux return path (e.g., as a distributed gap center post), it will not perform well by itself since part of the flux path would fall within a high-loss area. In contrast, both freeze-cast sample types

possess an improved quality factor in at least two directions, indicating that these samples will perform well also without the addition of high permeability materials in the flux return path (as opposed to the magnetically aligned Sendust-PDMS composite above).

Further performance improvements will be achieved with improved soft magnetic materials and flakes such as, smaller and thinner flakes, and perfectly flat flakes to minimize flake spacing and ensure a truly nacre-like alignment and slurries with optimized particle size distribution for optimal packing. Additionally, increasing magnetic flake volume fraction in the composite, will increase the permeability, and decrease the composites resistance. While increasing the magnetic flake fraction will also increase eddy currents and resulting losses, these effects can be counteracted through the use of smaller and thinner flakes and reduced flake spacings, to increase the permeability, and additionally further perfection in flake alignment, since the dissipated power is proportional to the square of the current, the current is proportional to the area of the eddy current loop, and the better the flakes are aligned parallel to B-field with their thin dimension, the lower the losses will be that result.

4. Conclusion

This systematic study of magnetic composites freeze cast from flake-based Sendust slurries in the presence and the absence of an externally applied, uniform B-field reveals that the flakes preferentially align with the freezing direction in the absence of the B-field, and with the B-field in its presence. When a uniform B-field is applied, a mono-domain structure forms, in which in addition to the flakes in the cell wall material also the ice-templated cell walls or lamellae are aligned parallel to the B-field. Simultaneously, both flakes and cell walls experience a weaker preferential alignment parallel to the freezing direction due to a shear flow that occurs because of the volumetric expansion of the ice phase and mold contraction during the directional solidification. However, the B-field force and particle-particle interactions

dominate and prevent a highly regular, nacre-like flake packing. The resulting orthotropic structure of the freeze-cast magnetic composite is in both cases reflected also in orthotropic mechanical and magnetic properties of the material. The magnetic composites manufactured by magnetic-field assisted freeze possesses by a factor of 2-4 times higher a stiffness, strength, and toughness than composites that were processed in the absence of a magnetic field and do not exhibit the same monodomain architecture. The highly aligned microstructure in the weakest direction perpendicular to both the freezing and the B-field directions eases composite compaction to at least 80% strain. Last but not least, magnetic freeze-casting offers two considerable advantages over other techniques for the alignment of magnetic flakes: magnetic composites for use in power transformation can be produced in bulk form, and most importantly, the freeze-cast magnetic composites achieve lower losses in two directions of flux excitation so that they can be used without an additional high permeability flux return path. Collated, the results presented in this study highlight the superior mechanical and magnetic material performance of achieved, when freeze casting magnetic flakes in an externally applied, uniform magnetic field.

5. Experimental Section

Magnetic Flake Slurry Preparation

To prepare the magnetic flake slurry, chitosan (low molecular weight, Sigma-Aldrich, MO, USA) was dissolved in 1% acetic acid in deionized water (Glacial, ACS grade, EMD Millipore) on a roller mixer to prepare a 3% w/v solution. Sendust flakes (Fe-Si-Al, 300 mesh, Chengdu Huarui Industrial Co., Ltd.) were added to the solution to prepare a 27% w/v slurry, which corresponds to a 9:1 mass ratio of magnetic flakes to chitosan binder. The slurry was homogenized with a high shear SpeedMixer (DAC 150 FVZ-K, FlackTek, Landrum, SC) for 90 s at 2000 rpm.

Magnetic Fixture to Achieve Uniform Magnetic Flux

In order to apply a uniform magnetic field to the slurry during freeze-casting, a magnetic fixture was custom-designed and built, in which neodymium permanent magnets (B884-N52, 52 MGOe, K&J Magnetics, Inc., Bucks County, PA) were placed on the sides of the fixture with their north poles oriented in the same direction, and sandwiched between Si-steel laminations across the top and bottom of the stack.

Magnetic-Field Assisted Freeze Casting

To freeze cast magnetic composites, an acrylic square mold of 25.4 mm (1 in) side length, 60 mm height and 1.59 mm (1/16 inch) wall thickness, sealed with a copper bottom plate, was filled to 35 mm height with the magnetic flake slurry, then placed in the custom-design magnetic fixture (Figure 7) and atop the temperature-controlled copper cold finger of a freeze caster, detailed in previous studies [21,23]. To directionally solidify the sample, the cold finger temperature was decreased at a constant applied cooling rate of 10°C/min until a temperature of -150°C was reached. Once fully frozen, the sample was removed from the cold finger, demolded with a punch, and lyophilized in a FreeZone 6 Freeze Dry System (Labconco, Kansas City, MO) for at least 72 hours at 0.008 mbar pressure and -85°C coil temperature.

Scanning Electron Microscopy (SEM) and Focused Ion Beam (FIB)

The architecture of the freeze-cast composites and the microstructure of the cell walls were characterized by scanning electron microscopy (SEM) (Vega 3, TESCAN, Czech Republic), and with a combined SEM-FIB (focused ion beam) system (Scios 2, FEI, Hillsboro, OR, USA). SEM micrographs were taken on the Vega 3 with an accelerating voltage of 5kV at a working distance of 10 mm. Cross-sections of individual cell walls were FIB-milled cutting

a wedge of 25 µm × 30 µm side length and 25 µm depth using a beam current of 7 nA for the bulk cut and 70pA for cleaning at an acceleration voltage of 30 kV, before imaging with the SEM with an accelerating voltage of 2kV and a beam current of 0.1nA.

X-ray Microtomography

The architecture of the freeze-cast magnetic composite was analyzed in 3D by X-ray microtomography performed with a Skyscan 1272 system (Bruker, Kontich, Belgium) using an X-ray source operated at 70kV and 142 µA with 0.5 mm Al filter. The pixel size was 4 µm after 2 × 2 binning. Radiographs of 2456 pixels × 1640 pixels were recorded, corresponding to a field of view of 9.8 mm × 6.6 mm. Rotating the sample at 0.6° step size from 0° to 360°, 600 projections were recorded per tomogram. Tomographic reconstructions were obtained with the NRecon software (Version 1.6.10.1, Bruker Kontich, Belgium). Volume renderings and sample cross-sections were created using Avizo 9.0 (FEI, Hillsboro, OR, USA).

Mechanical Testing

For mechanical testing, 5 mm cubes were cut with a diamond wire saw (Model 4240, WELL Diamond Wire Saws, Inc., Norcross, GA, USA) at a height of 17.5 mm measured from the sample bottom to the cube center. At least three cubes were tested for each composite sample and each of the different directions of compression. In the case of samples frozen without a magnetic field, the samples were tested with the force applied parallel (||FD) and perpendicular (⊥FD) to the freezing direction. In the case of samples frozen in the magnetic field, the mechanical properties were determined parallel to the freezing direction (||FD), and perpendicular to the freezing direction both parallel (||BF) and perpendicular (⊥FD⊥BF) to the magnetic field direction. Mechanical testing was carried out in compression on a universal

testing machine (Model 4442, Instron, Norwood, MA, USA) with a 50 N load cell and a cross head speed of 0.05 mm s^{-1}, corresponding to a strain rate of 0.01 s^{-1}.

Magnetic Performance Measurement

The magnetic performance was measured with a custom-designed magnetic impedance analyzer test fixture. Reference magnetic composite samples with randomly aligned flakes were used to verify the magnetic performance improvement effected by flake alignment. To produce the reference samples, Sendust flakes were thoroughly mixed with PDMS and allowed to cure for two days; both toroidal and cubical samples with randomly aligned flakes were prepared. Additionally, a flake-PDMS composite was created in which the flakes were aligned by attaching a permanent magnet to the mold during the entire cure time. The "Ref" traces are measurements of the randomly aligned flake-PDMS reference, and the "A", "B", and "C" traces of the cubic reference core were measurements in three different directions.

Open circuit calibration with no core inserted and end coils pushed together and load calibration with a reference sample of known permeability, $\mu_{r,ref}$, were performed to obtain best possible material characterization results. The reference material was composed of Sendust flakes randomly aligned in a PDMS binder. First, a toroid was formed from the material to measure $\mu_{r,ref}$ in a closed magnetic circuit, then a cubic sample was cut from the center of the toroid to calibrate the custom-designed magnetic impedance analyzer.

The quality factors of the flake-PDMS and the freeze-cast magnetic composite cores were measured from 10 kHz to 1 MHz with a custom-designed, capability-proven magnetic impedance measurement fixture based on an open magnetic circuit characterization method.[10] The 5 mm side-length freeze-cast composite cubes tested were cut as described in section 2.4 for the mechanical testing samples, and their quality factors determined along the same three

directions: parallel to the freezing direction, and perpendicular to the freezing direction both parallel and perpendicular to the magnetic field direction.

Acknowledgements

K.Y. and U.G.K.W. thank Jason Bice and Prof. Randall Erb at Northeastern University, USA, for their assistance with the magnetic field measurement, Dr. Yi Thomann, Max D. Mylo, and Prof. Thomas Speck at the University of Freiburg for their assistance with X-ray microtomography and FIB-SEM imaging, and the Shared Resources facilities (Electron Microscopy Facilities) at the Norris Cotton Cancer Center at Dartmouth College (NCI Cancer Center Support Grant 5P30 CA023108-37) for imaging support. The authors gratefully acknowledge financial support through NSF-CMMI Award 1538094, NSF-IUCRC Award 1822140, and NASA Award 80NSSC18K0305.

Received: ((will be filled in by the editorial staff))
Revised: ((will be filled in by the editorial staff))
Published online: ((will be filled in by the editorial staff))

References

[1] C. R. Sullivan, B. A. Reese, A. L. F. Stein, P. A. Kyaw, In *2016 International Symposium on 3D Power Electronics Integration and Manufacturing (3D-PEIM)*; 2016; pp. 1–23.

[2] A. J. Hanson, J. A. Belk, S. Lim, C. R. Sullivan, D. J. Perreault, *IEEE Transactions on Power Electronics* **2016**, *31*, 7909.

[3] Y. Zhou, X. Kou, M. Mu, B. M. McLaughlin, X. Chen, P. E. Parsons, H. Zhu, A. Ji, F. C. Lee, J. Q. Xiao, *Journal of Applied Physics* **2012**, *111*, 07E329.

[4] T. Suetsuna, S. Suenaga, K. Harada, *Scripta Materialia* **2016**, *113*, 89.

[5] Y. Shirakata, N. Hidaka, M. Ishitsuka, A. Teramoto, T. Ohmi, *IEEE Transactions on Magnetics* **2008**, *44*, 2100.

[6] D. Roy, P. S. Anil Kumar, *Journal of Applied Physics* **2012**, *111*, 07A315.

[7] S. Yoshida, S. Ando, Y. Shimada, K. Suzuki, K. Nomura, K. Fukamichi, *Journal of Applied Physics* **2003**, *93*, 6659.

[8] Y. Endo, H. Sato, T. Miyazaki, M. Yamaguchi, H. Kamada, M. Takahashi, M. Sakamoto, S. Maita, N. Kato, Y. Yorozu, T. Yasui, In *2015 IEEE International Magnetics Conference (INTERMAG)*; 2015; pp. 1–1.

[9] Y. Endo, H. Sato, T. Miyazaki, M. Yamaguchi, H. Kamada, M. Takahashi, M. Sakamoto, S. Maita, N. Kato, Y. Yorozu, T. Yasui, *IEEE Transactions on Magnetics* **2015**, *51*, 1.

[10] B. A. Reese, C. R. Sullivan, U. G. Wegst, In *2018 IEEE International Magnetics Conference (INTERMAG)*; 2018; pp. 1–1.

[11] I. Nelson, T. A. Ogden, S. A. Khateeb, J. Graser, T. D. Sparks, J. J. Abbott, S. E. Naleway, *Advanced Engineering Materials* **2019**, *21*, 1801092.

[12] P. Niksiar, F. Y. Su, M. B. Frank, T. A. Ogden, S. E. Naleway, M. A. Meyers, J. McKittrick, M. M. Porter, *Ceramics* **2019**, *2*, 208.

[13] I. Nelson, L. Gardner, K. Carlson, S. E. Naleway, *Acta Materialia* **2019**, *173*, 106.

[14] I. Nelson, J. Varga, P. Wadsworth, M. Mroz, J. J. Kruzic, O. T. Kingstedt, S. E. Naleway, *JOM* **2020**, *72*, 1498.

[15] I. Nelson, S. E. Naleway, *Journal of Materials Research and Technology* **2019**.

[16] M. M. Porter, M. Yeh, J. Strawson, T. Goehring, S. Lujan, P. Siripasopsotorn, M. A. Meyers, J. McKittrick, *Materials Science and Engineering: A* **2012**, *556*, 741.

[17] P. Niksiar, M. B. Frank, J. McKittrick, M. M. Porter, *Journal of Materials Research and Technology* **2019**, *8*, 2247.

[18] M. B. Frank, S. E. Naleway, T. Haroush, C.-H. Liu, S. H. Siu, J. Ng, I. Torres, A. Ismail, K. Karandikar, M. M. Porter, O. A. Graeve, J. McKittrick, *Materials Science and Engineering: C* **2017**, *77*, 484.

[19] M. B. Frank, S. Hei Siu, K. Karandikar, C.-H. Liu, S. E. Naleway, M. M. Porter, O. A. Graeve, J. McKittrick, *Journal of the Mechanical Behavior of Biomedical Materials* **2017**, *76*, 153.

[20] S. Deville, E. Saiz, R. K. Nalla, A. P. Tomsia, *Science* **2006**, *311*, 515.

[21] U. G. K. Wegst, M. Schecter, A. E. Donius, P. M. Hunger, *Philosophical Transactions of the Royal Society A: Mathematical, Physical and Engineering Sciences* **2010**, *368*, 2099.

[22] P. M. Hunger, A. E. Donius, U. G. K. Wegst, *Acta Biomaterialia* **2013**, *9*, 6338.

[23] P. M. Hunger, A. E. Donius, U. G. K. Wegst, *Journal of the Mechanical Behavior of Biomedical Materials* **2013**, *19*, 87.

[24] U. G. K. Wegst, H. Bai, E. Saiz, A. P. Tomsia, R. O. Ritchie, *Nature Materials* **2015**, *14*, 23.

[25] R. M. Erb, J. J. Martin, R. Soheilian, C. Pan, J. R. Barber, *Advanced Functional Materials* **2016**, *26*, 3859.

[26] R. Soheilian, H. Abdi, C. E. Maloney, R. M. Erb, *Journal of Colloid and Interface Science* **2018**, *513*, 400.

[27] R. M. Erb, R. Libanori, N. Rothfuchs, A. R. Studart, *Science* **2012**, *335*, 199.

[28] J. J. Martin, B. E. Fiore, R. M. Erb, *Nature Communications* **2015**, *6*, 1.

[29] Z. M. Sherman, J. L. Pallone, R. M. Erb, J. W. Swan, *Soft Matter* **2019**, *15*, 6677.

[30] M. R. Sommer, R. M. Erb, A. R. Studart, *ACS Appl. Mater. Interfaces* **2012**, *4*, 5086.

[31] Z. Lin, Y. Liu, S. Raghavan, K. Moon, S. K. Sitaraman, C. Wong, *ACS Appl. Mater. Interfaces* **2013**, *5*, 7633.

[32] R. M. Erb, H. S. Son, B. Samanta, V. M. Rotello, B. B. Yellen, *Nature* **2009**, *457*, 999.

[33] D. van der Beek, A. V. Petukhov, P. Davidson, J. Ferré, J. P. Jamet, H. H. Wensink, G. J. Vroege, W. Bras, H. N. W. Lekkerkerker, *Phys. Rev. E* **2006**, *73*, 041402.

[34] H. Le Ferrand, F. Bouville, T. P. Niebel, A. R. Studart, *Nature Materials* **2015**, *14*, 1172.

[35] R. Libanori, R. M. Erb, A. R. Studart, *ACS Appl. Mater. Interfaces* **2013**, *5*, 10794.

[36] R. M. Erb, J. Segmehl, M. Charilaou, J. F. Löffler, A. R. Studart, *Soft Matter* **2012**, *8*, 7604.

[37] R. M. Erb, J. Segmehl, M. Schaffner, A. R. Studart, *Soft Matter* **2013**, *9*, 498.

[38] C. Yuan, B. Duan, L. Li, B. Xie, M. Huang, X. Luo, *ACS Appl. Mater. Interfaces* **2015**, *7*, 13000.

[39] R. M. Erb, J. S. Sander, R. Grisch, A. R. Studart, *Nature Communications* **2013**, *4*, 1.

[40] L. J. Gibson, M. F. Ashby, *Cellular Solids: Structure and Properties*; Cambridge University Press, 1999.

[41] B. R. Jennings, K. Parslow, R. H. Ottewill, *Proceedings of the Royal Society of London. A. Mathematical and Physical Sciences* **1988**, *419*, 137.

[42] G. P. Arrighini, M. Maestro, R. Moccia, *J. Chem. Phys.* **1968**, *49*, 882.

[43] L. Otero, A. C. Rodríguez, M. Pérez-Mateos, P. D. Sanz, *Comprehensive Reviews in Food Science and Food Safety* **2016**, *15*, 646.

[44] M. F. Ashby, *Philosophical Transactions of the Royal Society A: Mathematical, Physical and Engineering Sciences* **2006**, *364*, 15.

[45] Y. Imaida, M. Takagawa, T. Kirimura, K. Hirota, O. Yamaguchi, A. Kakitsuji, H. Miyamoto, *Materials Research Bulletin* **1992**, *27*, 661.

[46] M. T. Abba, P. M. Hunger, S. R. Kalidindi, U. G. K. Wegst, *Journal of the Mechanical Behavior of Biomedical Materials* **2016**, *55*, 140.

[47] P. M. Hunger, Structure-Property-Processing Correlations in Freeze-Cast Hybrid Scaffolds. Ph.D., Drexel University: United States -- Pennsylvania, 2011.

Table of Contents Entry

Magnetic Sendust flake-chitosan composites with an orthotropic, nacre-like hierarchical microstructure and exceptional mechanical and magnetic properties are fabricated by freeze casting in a uniform magnetic field. The resulting excellent permeability and quality factor and high mechanical properties along two directions of the composites make them highly promising low loss candidates for power conversion applications.

Kaiyang Yin, Bradley A. Reese, Charles R. Sullivan, and Ulrike G.K. Wegst*

Superior Mechanical and Magnetic Performance of Highly Anisotropic Sendust Flake Composites Freeze Cast in a Uniform Magnetic Field

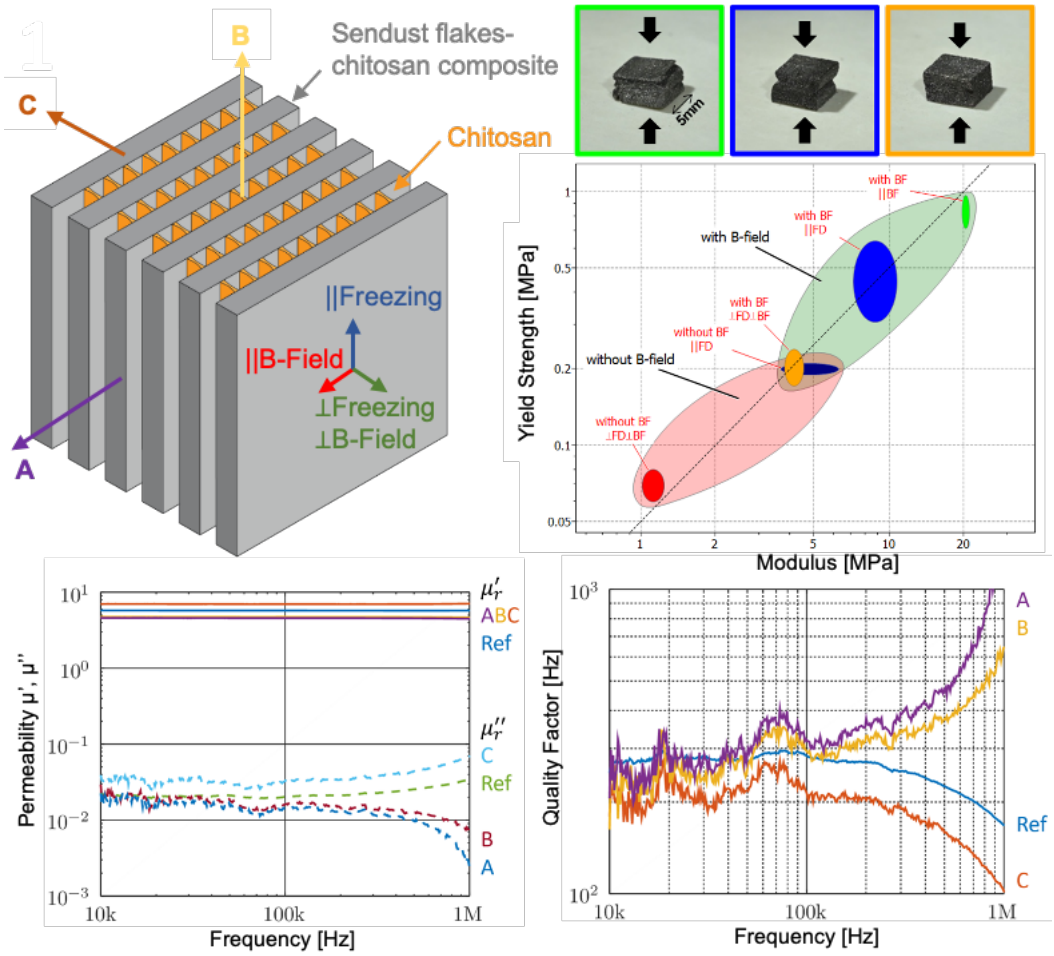

Supporting Information

Superior Mechanical and Magnetic Performance of Highly Anisotropic Sendust Flake Composites Freeze Cast in a Uniform Magnetic Field

*Kaiyang Yin, Bradley A. Reese, Charles R. Sullivan, and Ulrike G.K. Wegst**

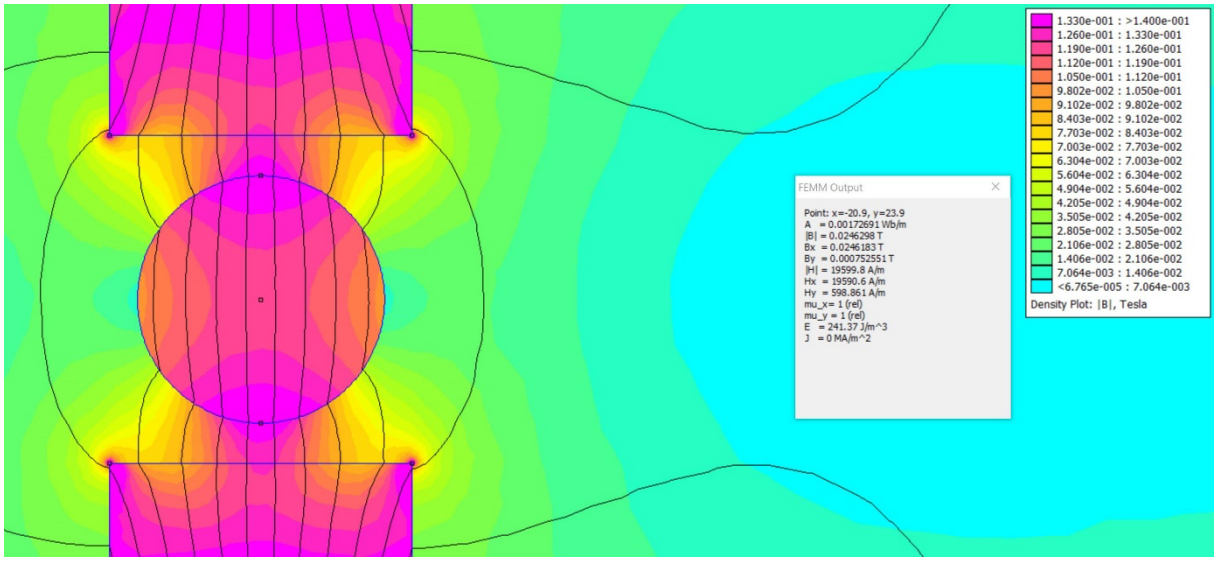

Figure S1. Finite element analysis (FEA) of round mold. The estimated minimum and maximum flux density in the sample area are 98 mT (sides facing the magnets) and 130 mT (sides not facing the magnets), respectively.